

Influence of Population III stars on cosmic chemical evolution

E. Rollinde^{1*}, E. Vangioni^{1*}, D. Maurin^{2,1*}, K. A. Olive^{3*}, F. Daigne^{1*†}, J. Silk^{1,4*},
and F. H. Vincent^{1*}

¹*Institut d'Astrophysique de Paris, UMR7095 CNRS, Université Pierre et Marie Curie, 98 bis bd Arago, 75014 Paris, France*

²*Laboratoire de Physique Nucléaire et Hautes Energies, CNRS-IN2P3/Universités Paris VI et Paris VII, 4 place Jussieu, Tour 33, 75252 Paris Cedex 05, France*

³*William I. Fine Theoretical Physics Institute, School of Physics and Astronomy, University of Minnesota, Minneapolis, MN 55455, USA*

⁴*Department of Physics, Oxford University, Keble Road, Oxford OX1 3RH, UK*

Accepted XXXX. Received XXXX; in original form XXXX

ABSTRACT

New observations from the Hubble ultra deep field suggest that the star formation rate at $z > 7$ drops off faster than previously thought. Using a newly determined star formation rate for the normal mode of Population II/I stars (PopII/I), including this new constraint, we compute the Thomson scattering optical depth and find a result that is marginally consistent with WMAP5 results. We also reconsider the role of Population III stars (PopIII) in light of cosmological and stellar evolution constraints. While this input may be needed for reionization, we show that it is essential in order to account for cosmic chemical evolution in the early Universe. We investigate the consequences of PopIII stars on the local metallicity distribution function of the Galactic halo (from the recent Hamburg/ESO survey of metal-poor stars) and on the evolution of abundances with metallicity (based on the ESO large program on very metal-poor stars), with special emphasis on carbon-enhanced metal-poor stars. The metallicity distribution function shape is well reproduced at low iron abundance ($[\text{Fe}/\text{H}] \gtrsim -4$), in agreement with other studies. However, the Hamburg/ESO survey hints at a sharp decrease of the number of low-mass stars at very low iron abundance, which is not reproduced in models with only PopII/I stars. The presence of PopIII stars, of typical masses 30–40 M_{\odot} , helps us to reproduce this feature, leading to a prompt initial enrichment before the onset of PopII/I stars. The metallicity at which this cut-off occurs is sensitive to the lowest mass of the massive PopIII stars, which makes the metallicity distribution function a promising tool to constrain this population. Our most important results show that the nucleosynthetic yields of PopIII stars lead to abundance patterns in agreement with those observed in extremely metal-poor stars. This can be demonstrated by the transition discriminant (a criterion for low-mass star formation taking into account the cooling due to C II and O I). In this chemical approach to cosmic evolution, PopIII stars prove to be a compulsory ingredient, and extremely metal-poor stars are inevitably born at high redshift.

Key words: nucleosynthesis, abundances – methods: statistical – stars: abundances, chemically peculiar, formation – cosmology: miscellaneous.

1 INTRODUCTION

Recent data from the Hubble Ultra Deep Field (HUDF) have allowed the determinations of the cosmic star formation rate (SFR) to be extended from redshifts $z \sim 4$ up to $z \sim 7 - 8$ (Bouwens et al. 2007). In the context of the Λ CDM model, which has by and large been confirmed by the observation of anisotropies in the diffuse cosmological microwave background (CMB) by WMAP (Spergel et al. 2007; Dunkley et al. 2009), a remaining

challenge lies in understanding the first structures, including galaxies and stars. This step requires either direct observations (of black holes, gamma-ray bursts...) or indirect constraints through luminosity functions, metal pollution and relic metal-poor stars (e.g. Tumlinson 2006; Salvadori et al. 2007). Our work develops the latter approach, and focuses on the nucleosynthesis pollution from the first stars and their consequences for relic metal-poor stars.

The role of massive PopIII stars as ionization sources at high redshift is poorly understood. Indeed, their role has been clouded by the fact that the measured value of the Thomson scattering optical depth (from $z = 0$ to the redshift of emission of the CMB) has decreased significantly from WMAP1 to WMAP5. Current measurements imply a redshift for an instantaneous reionization

* E-mail: rollinde@iap.fr (ER); vangioni@iap.fr (EV); dmaurin@lphne.in2p3.fr (DM); olive@physics.umn.edu (KAO); daigne@iap.fr (FD); silk@astro.ox.ac.uk (JS); vincentf@iap.fr (FHV)

† Institut Universitaire de France.

of $z = 11.0 \pm 1.4$ ($\tau = 0.087 \pm 0.017$) (Dunkley et al. 2009). In this context, the new observations of the cosmic SFR at high redshift bring a fresh perspective on the role played by PopIII stars. Since PopIII stars have a very specific impact on nucleosynthesis, it is useful to incorporate constraints from stellar observations. From the nucleosynthetic point of view, halo stars have long been used to constrain galactic chemical evolution models, but were quite disconnected from cosmological models. Yet PopIII stars might be the primary source for the early metal enrichment of the interstellar medium (ISM) as well as for the intergalactic medium (IGM). The different abundance patterns observed in extreme metal-poor stars (EMPS) may well be explained in terms of these stars (Yoshida et al. 2007; Frebel 2008a). It has been shown (Bromm & Loeb 2003) that the abundances of ionized carbon and neutral atomic oxygen are important for the transition from PopIII to PopII/I. Frebel et al. (2007) have defined a transition discriminant, D_{trans} , and we show below that this quantity clearly reveals the nucleosynthetic imprint of PopIII stars.

The paper is organized as follows. In Section 2, we summarize our model for the global chemical and cosmic evolution. New constraints related to the SFR and reionization are described in Section 3. We first reconsider the reionization constraint from WMAP5 data in terms of a single normal mode of PopII/I star formation, by fitting the SFR to the most recent data (Bouwens et al. 2007). We compare this result to a model which includes a contribution from PopIII stars. Stellar observations are described in Section 4. To address these issues, we use some of the abundances (Fe, O, C, Si) of individual stars of the European Southern Observatory Large Program (ESO-LP) ‘First Stars’ (Cayrel et al. 2004) and of peculiar extremely-low metallicity stars. We also compute the metallicity distribution function (MDF, number of observed low-mass stars at a specific metallicity) and compare this to recent observations (Schoerck et al. 2008). A grid study of the model parameters allows us to draw confidence contours for the SFR of PopIII stars and on the transition discriminant in Section 5. We also consider abundances derived from 1D and 3D model atmospheres and compare results in each case. Our best model is used as an illustration in Sections 3 and 4. We summarize our results and conclude in Section 6.

2 A GLOBAL COSMIC EVOLUTIONARY MODEL

Any model for star formation in a cosmological context requires the inclusion of a model for dark matter structure formation, accretion and outflow of baryonic matter. Numerical simulations consistently follow the dark matter and baryonic components. Merger trees have also been used extensively. These models have the ability to probe different IMFs and critical metallicities. However, as yet, none of these methods follow individual element abundances. In a complementary approach, we have developed a detailed model of cosmological chemical evolution (Daigne et al. 2006), using a simplified description of non linear structures, based on the standard Press-Schechter (PS) formalism (Press & Schechter 1974; Jenkins et al. 2001; Sheth & Tormen 1999).

One of the main advantages over semi-analytical or fully resolved simulations (that take up a lot of computer time) is the ability to probe a large region of parameter space and to follow abundances of individual elements (we use only Fe, C and O abundances in this study). Such simplified models are successfully used to tackle specific questions related to early star formation and reionization (Kampakoglou et al. 2008; Henriques et al. 2009; Bagla et al.

2009). These models only give average quantities, but they can reproduce all salient features of semi-analytical approaches. They are also supported by the lack of scatter in chemical observations of stars, and the fact that the MDF from Galactic halo field stars is statistically very similar to that of Galactic globular cluster systems and the stellar population of the nearest dSph satellites of the Galaxy (Schoerck et al. 2008; Kirby et al. 2008; Frebel et al. 2009). However, note that the Galactic globular cluster MDF drops to zero at $[\text{Fe}/\text{H}] = -2.4$. Presently, it is unclear where the cut-off is for the stellar population of dSph.

We consider two distinct modes of star formation: a normal mode of PopII/I and a massive mode of PopIII stars. The observed SFR and element abundances at redshift $z \lesssim 6$ (Section 4) are accommodated by the normal mode with a Salpeter IMF (Daigne et al. 2006), while the WMAP5 integrated optical depth is marginally reproduced (Section 3). For PopIII stars, we perform a grid analysis of a few key parameters to check their relevance for the chemical abundances of very metal-poor stars. Throughout this paper, a primordial power spectrum with a power law index $n = 1$ is assumed and we adopt the cosmological parameters of the so-called concordance model (Spergel et al. 2007; Dunkley et al. 2009), i.e. $\Omega_m = 0.27$, $\Omega_\Lambda = 0.73$, $h = 0.71$ and $\sigma_8 = 0.9$.

2.1 Description of the model

Baryons are divided into three reservoirs. Two reservoirs account for the matter in collapsed structures: the gas (hereafter ‘ISM’) and the stars and their remnants (hereafter ‘stars’). The third reservoir represents baryons in the medium between these structures (hereafter ‘IGM’). The evolution of the mass of each reservoir is governed by equations (1) and (2) in Daigne et al. 2006 (see also figure 1 in the same paper), which depend on different fluxes: (i) baryon accretion from the IGM to the ISM, due to the structure formation process. This term is computed at each redshift in the framework of the Press & Schechter formalism (see equation (6) in Daigne et al. 2006), assuming that collapsed structures correspond to dark matter halos with a minimum mass M_{min} (which, for simplicity, is kept constant over the entire evolution); (ii) baryon ejection from the ISM into the IGM, associated with outflows from the collapsed structures. Such outflows are powered by a fraction ϵ of the kinetic energy released by SN explosions. The corresponding mass flux is evaluated by assuming that the typical velocity of these outflows scales as the mean escape velocity at redshift z . This velocity is computed by averaging the escape velocity over the distribution of the mass of dark matter halos above M_{min} at redshift z . Outflows become less efficient with time as the typical mass of collapsed structures increases; (iii) the third flux is associated with the star formation process and transfers baryons from the ISM to stars. It can easily be computed once a star formation rate $\Psi(z)$ has been specified. Our assumptions regarding this SFR are detailed below; (iv) the final flux stands for mass ejection from stars to the ISM, associated with stellar winds and explosions. It is computed from the SFR and the IMF. We do not assume instantaneous recycling and therefore take into account the lifetimes of stars. The stellar data we use are described in the next subsection and are dependent on both the initial mass and metallicity of the stars.

In addition to the evolution of the mass, we also compute the chemical evolution in the ‘ISM’ and the ‘IGM’. For any chemical element i , the mass fractions in the ISM and the IGM, X_i^{ISM} and X_i^{IGM} , are followed as a function of the redshift. The corresponding differential equations can be found in Daigne et al. 2004 (equations (6) and (7)) and are derived from the previous mass fluxes

assuming that (i) the chemical composition of the accretion flow related to the structure formation process is the composition of the IGM at redshift z ; (ii) the chemical composition of the outflows escaping collapsed structures is the composition of the ISM at redshift z ; (iii) this composition is also the composition of stars that form at the same redshift; (iv) finally the composition of the matter ejected by stars into the ISM is given by stellar yields. These yields are detailed in the next subsection. Once the chemical evolution is known, it can be inverted to estimate the redshift of formation of a star from its observed abundance, as explained in Section 5.1.2.

The models considered here are bimodal. Each model contains a normal mode with stellar masses between $0.1 M_{\odot}$ and $100 M_{\odot}$, with an IMF with a near Salpeter slope. The SFR of the normal mode peaks at $z \approx 3$. In addition, we allow for a massive component, which dominates star formation at high redshift. We primarily focus on stars with $40\text{--}100 M_{\odot}$, which terminate as type II supernovae. The nucleosynthetic pattern of pair-instability SN (PISN) is briefly commented on in the conclusions.

In addition to the SFR, the IMF and stellar data, this simple model introduces only two other parameters: the minimum mass of the dark matter halo in collapsed structures, M_{\min} , and the efficiency of supernovae to power outflows from collapsed structures, ϵ . The impact of these two parameters has been discussed in detail in Daigne et al. 2006. In the present paper, we adopt a typical scenario with $M_{\min} = 10^7 M_{\odot}$ and $\epsilon = 3 \times 10^{-3}$. This minimum mass, M_{\min} , is also deduced from hydrodynamical simulations at $z \sim 15$. Note that Johnson et al. (2009) consider $M_{\min} = 10^8 M_{\odot}$ at $z = 12.5$ (see also Daigne et al. 2006; Bagla et al. 2009; Trenti & Stiavelli 2009). ϵ primarily impacts on the enrichment of IGM, which is not considered in this paper.

2.2 Yields and lifetimes

The lifetimes of intermediate mass stars ($0.9 < M/M_{\odot} < 8$) are taken from Maeder & Meynet (1989) and from Schaerer (2002) for more massive stars. Old halo stars with masses below $\sim 0.9 M_{\odot}$ have a lifetime long enough to be observed today. They inherit the abundances of the ISM at the time of their formation. Thus, their observed abundances reflect, in a complex way (due to exchanges with the IGM), the yields of all massive stars that have exploded earlier.

The yields of stars depend on their mass and their metallicity, but not on their status (i.e. PopII/I or PopIII). Some PopII/I stars are massive, although in only a very small proportion since we use a steep Salpeter IMF. PopIII stars are all very massive stars. We use the tables of yields (and remnant types) given in van den Hoek & Groenewegen (1997) for intermediate mass stars ($< 8 M_{\odot}$), and the tables in Woosley & Weaver (1995) for massive stars ($8 < M/M_{\odot} < 40$). An interpolation is made between different metallicities ($Z=0$ and $Z=10^{-4}, -3, -2, -1, 0 Z_{\odot}$) and we extrapolate the tabulated values beyond $40 M_{\odot}$.

Heger & Woosley (2008) have provided new stellar yields in the mass range $10 - 100 M_{\odot}$, but only at zero-metallicity. At zero-metallicity, and in the $40 - 100 M_{\odot}$ mass range, we have checked that our extrapolated values are consistent with those yields. Indeed, their favored model corresponds to very little mixing and a high oxygen to iron ratio, in agreement with the Woosley & Weaver (1995) model we chose. We explicitly checked that our results were not modified using either Woosley & Weaver (1995) or Heger & Woosley (2008) at zero-metallicity.

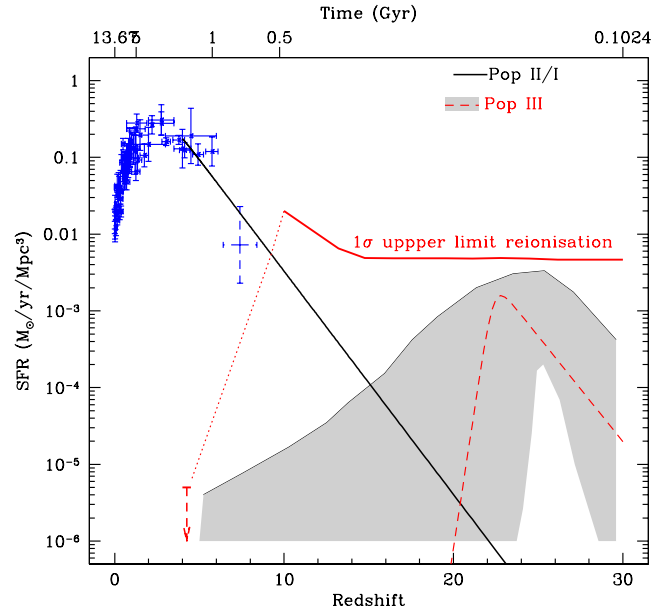


Figure 1. Cosmic SFR as a function of redshift. *PopII/I*: The observed SFR up to $z \sim 5$ (solid blue points) is taken from Hopkins & Beacom (2006). The dashed blue data point comes from Bouwens et al. (2007). The solid black line is the extrapolated PopII/I SFR, using the shape given by Eq. (1), in order to match the data at $z \lesssim 5$ and the upper limit at $z \sim 7$. *PopIII*: The recent non-observation of Ly α -HeII dual emitters (Nagao et al. 2008) at $z \sim 4 - 4.5$ is shown with the red arrow. The red line corresponds to the PopIII SFR upper limit, adjusted to satisfy the 1σ WMAP5 upper limit on the Thomson optical depth (see Fig. 2). This limit has to drop (dotted line) to be reconciled with the Ly α -HeII observation. The envelope (shaded area) contains all models, that reproduce the D_{trans} evolution at a 95% CL (see Section 5 and Fig. 4) For illustration, the best model for the PopIII SFR (including nucleosynthetic and cosmological constraints, described in Section 4) is shown by the dashed red line. This SFR is parametrized with Eq. (1), with the following parameters: $\nu_{\text{III}} = 0.0016 M_{\odot} \text{ yr}^{-1} \text{ Mpc}^{-3}$ (astration rate for PopIII stars), $z_{\text{m III}} = 22.8$, $a_{\text{III}} = 4$ and $b_{\text{III}} = 3.3$.

3 COSMOLOGICAL CONSTRAINTS

Taking into account the results of recent observations on the PopII/I SFR (Bouwens et al. 2007), we reanalyse the reionization capability of these stars. The WMAP5 upper limit on the Thomson optical depth is then used to set constraints on the PopIII SFR.

3.1 PopII/I SFR

We fit the SFR history of PopII/I stars to the data compiled in Hopkins & Beacom (2006) (from $z = 0$ to 5), and to the recent measurement at $z \sim 7$ by Bouwens et al. (2007) (see Fig. 1). The behaviour of the SFR at high redshift is still disputed. Some indirect measurements hint against a decline of the SFR beyond $z \sim 3$ (Faucher-Giguère et al. 2008), but direct observations of z_{850} -dropout galaxies seem to confirm a sharp decrease of the SFR at $z \sim 6-7$ (Oesch et al. 2009). The low level of the Bouwens et al. (2007) data thus places strong constraints on the PopII/I SFR.

The fit for the SFR, $\psi(z)$, is based on the mathematical form proposed in Springel & Hernquist (2003):

$$\psi(z) = \nu \frac{a \exp(b(z - z_m))}{a - b + b \exp(a(z - z_m))}. \quad (1)$$

The amplitude (astration rate) and the redshift of the SFR maximum are given by ν and z_m respectively, while b and $b - a$

are related to its slope at low and high redshifts respectively. In the following, we use the subscripts II/I and III for parameters related to PopII/I and PopIII SFRs respectively. The thick black curve in Fig. 1 is computed with $\nu_{\text{II/I}} = 0.3 \text{ M}_{\odot} \text{ yr}^{-1} \text{ Mpc}^{-3}$, $z_{\text{m II/I}} = 2.6$, $a_{\text{II/I}} = 1.9$ and $b_{\text{II/I}} = 1.2$. The parameter values chosen here differ from that in Greif & Bromm (2006) so as to better account for the high redshift data point (Bouwens et al. 2007). To be conservative with respect to the reionization constraint (see below), we choose a SFR consistent with the 1σ upper limit of this $z = 7$ observation. A steeper slope only decreases the number of ionizing photons.

3.2 Reionization from PopII/I stars

Having set the SFR in our model, we now compute the electron scattering optical depth for our choice of IMF. The evolution of the volume filling fraction of ionized regions is given by:

$$\frac{dQ_{\text{ion}}(z)}{dz} = \frac{1}{n_{\text{b}}} \frac{dn_{\text{ion}}(z)}{dz} - \alpha_{\text{B}} n_{\text{b}} C(z) \times Q_{\text{ion}}^2(z) (1+z)^3 \left| \frac{dt}{dz} \right|, \quad (2)$$

where n_{b} is the comoving density in baryons, $n_{\text{ion}}(z)$ the comoving density of ionizing photons, α_{B} the recombination coefficient, and $C(z)$ the clumping factor. This factor is taken from Greif & Bromm (2006) and varies from a value of 2 at $z \leq 20$ to a constant value of 10 for $z < 6$. The escape fraction, f_{esc} , is set to 0.2 for both PopIII and PopII/I SN, while Greif & Bromm (2006) take two different values. The number of ionizing photons for massive stars is calculated using the tables given in Schaerer (2002). Finally, the Thomson optical depth is computed as in Greif & Bromm (2006):

$$\tau = c\sigma_{\text{T}} n_{\text{b}} \int_0^z dz' Q_{\text{ion}}(z') (1+z')^3 \left| \frac{dt}{dz'} \right|, \quad (3)$$

where z is the redshift of emission, and σ_{T} the Thomson scattering cross-section.

In the upper panel of Fig. 2, we show the predicted evolution of the volume filling factor of ionized regions, Q_{ion} as a function of redshift. In the lower panel, we show the integrated optical depth from $z = 0$ to z . These results can be compared to Fig. 5 of Greif & Bromm (2006). We see that the normal mode (black solid curve) is contained in the 1σ WMAP limit (grey band) for the observed value for the Thomson optical depth.

3.3 Reionization from PopIII stars

A massive PopIII mode at high redshift makes it easier to reproduce the optical depth at high redshift. For illustrative purposes, the history of reionization is shown in Fig. 2 for a typical SFR (red dashed line in Fig. 1) found to best meet the local constraints (discussed in Section 5). The parameters of the best fit model for PopIII SFR are given in the caption of Fig. 1. The associated history of reionization is consistent with a two-step model of reionization as invoked in Dunkley et al. (2009), who also comment that *the WMAP5 data suggests a more gradual process with reionization beginning perhaps as early as 20*. In particular, the PopIII SFR allows $Q_{\text{ion}} \neq 0$ at $z > 10$. The bimodal SFR is consistent with recent general scenarios that have emerged from hydrodynamic simulations and analytical calculations (e.g. Bromm & Larson 2004; Greif et al. 2008). These studies have shown that, due to the re-collapse of the structures after disruption by massive SNe, low-mass star formation may

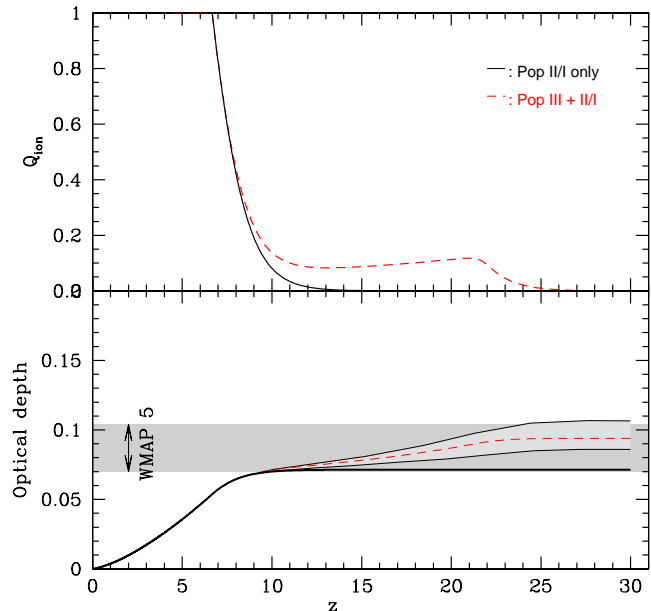


Figure 2. Histories of volume filling fraction of ionized regions, Q_{ion} (top panel) and the implied optical depth (lower panel) with and without PopIII stars (dashed red and solid black respectively). The envelope in the lower panel (light shaded area) shows the maximum and minimum values of optical depth reached by the different models that reproduce the chemical abundance constraints at a 95% CL (see Section 5). The lower panel also shows the range of allowed values for the optical depth as measured by WMAP5 (Dunkley et al. 2009).

have been delayed by more than a Hubble time or up to a redshift ~ 10 . This can be understood as a statistical description of the mechanical feedback implemented in merger trees (Salvadori et al. 2007) where a time delay between PopIII and PopII/I appears at each individual branch.

Using a grid analysis on the parameters of Eq. (1) for PopIII stars (see details in Section 5), we are able to derive an upper limit on the SFR. There is no lower limit as PopII/I stars alone are consistent with the WMAP reionization lower limit. The 68% CL upper limit on the SFR is reported as a solid red line in Fig. 1 that we stop below $z < 10$. At lower redshift, the most stringent constraint is set by the recent non-observation of Ly α -HeII dual emitters (Nagao et al. 2008), which gives an upper limit for the PopIII SFR of $5 \cdot 10^{-6} \text{ M}_{\odot} \text{ yr}^{-1} \text{ Mpc}^{-3}$ at $z \sim 4 - 4.5$ (red arrow). The dotted line reconciles this observational constraint with the WMAP5 upper limit. Note that within the region allowed by the cosmological constraint (bottom right), the shape of the SFR of PopIII remains completely unspecified (based on the reionisation constraint), as the relevant quantity is related to the integral over z of the SFR. We show in the following section that local observations require the existence of PopIII stars, and set stronger constraints on the SFR and its lower limit.

4 LOCAL OBSERVATIONS

The average mass of the structures in the PS formalism is close to the total mass of the Milky Way ($10^{12} \text{ M}_{\odot}$) at $z = 3$, which corresponds to the epoch of the peak of the global SFR. Our average description of the cosmic history is thus expected to be representative of the evolution of the Galaxy. In this section, local observations are analyzed in a global cosmological context.

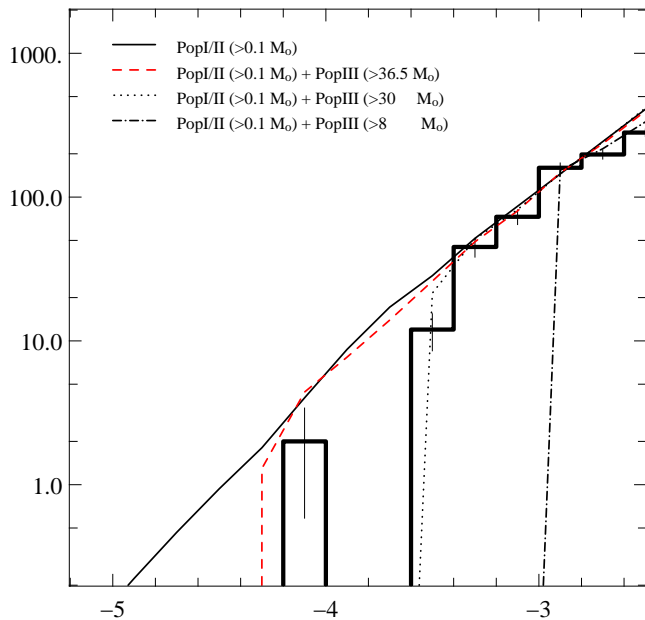


Figure 3. Comparison of the observed MDF (Schoerck et al. 2008, thick histogram) for the galactic halo stars with model calculations of the normal mode of star formation (black solid line). Other lines show the effect of the inclusion of PopIII stars with different mass ranges. All distributions are normalized to match the observations at $[Fe/H]=-3$.

4.1 Metallicity Distribution Function (MDF)

The MDF is the distribution of stars at a given iron abundance, derived from observations that have been corrected for various technical and observational biases. It has been recently published by the Hamburg-ESO survey (Schoerck et al. 2008) using the Christlieb et al. (2008) catalog. The thick line histogram in Fig. 3 is taken from Schoerck et al. (2008). As noted there, in order to compare observed and predicted MDF, one has to take into account the modification of the shape of the MDF by the selection of metal-poor candidates. Consequently, a comparison to our prediction is valid for $[Fe/H] < -2.5$ only¹.

In our analysis, for a given model (SFR and IMF of PopII/I and PopIII), we count the number of low mass stars created at each redshift. As the iron abundance in the ISM is also calculated as a function of the redshift, the metallicity of the stellar population at each redshift is known (Section 2.1). The value of the MDF in a given iron abundance bin, is given by the number of stars that are still shining today and were created at times when the iron abundance was within this bin. The MDF for several possible PopIII star formation histories are plotted along with the observation in Fig. 3. The solid black line corresponds to the normal mode, i.e. a Salpeter IMF starting at $0.1 M_{\odot}$. A massive mode is then added with a Salpeter IMF with different lower masses: $36.5 M_{\odot}$ (red dashed), $30 M_{\odot}$ (black dotted) and $8 M_{\odot}$ (black dot-dashed). The minimum mass of $36.5 M_{\odot}$ corresponds to our best model. Note that the value of the upper limit of the IMFs is not a key parameter, in contrast to the lower one, due to the steep slope of the IMF.

For $-4 < [Fe/H] < -2.5$, the slope of the MDF is well reproduced by PopII alone. The reality of the drop observed at $[Fe/H] \sim -3.6$ (compare the thin solid black line to the thick black

histogram) is still debated (e.g., Komiya et al. 2009). The prediction of several models for the MDF is discussed in Schoerck et al. (2008), where the authors conclude that none of them are able to explain the tail at $[Fe/H] < -4$, except a stochastic enrichment model (e.g. Karlsson 2006). In our model, as in Karlsson’s model, the presence of a massive mode implies the early production of iron, which has an impact on the low metallicity MDF: very few low mass stars at zero or quasi-null metallicity are expected in such a scenario, i.e., effectively as a prompt initial enrichment (PIE). The cut-off on the MDF at low metallicity depends on the lower mass of the massive mode.

Given the paucity of stars with $[Fe/H] \lesssim -3.5$, it is difficult to accurately discriminate between different star formation histories presently. Indeed, PopIII stars do not modify the MDF at $-3.5 < [Fe/H] < -2.5$, as long as their minimal mass is larger than about $30 M_{\odot}$.

4.2 Global nucleosynthetic evolution

We now focus on the giants of the ESO-LP (Cayrel et al. 2004) which contain the abundances of 17 elements from C to Zn for all of the observed stars. Following the nomenclature proposed in Beers & Christlieb (2005), very metal-poor (VMP) stars correspond to a metallicity $[Fe/H] < -2$, extremely metal-poor (EMP) stars to $[Fe/H] < -3$, ultra metal-poor (UMP) stars to $[Fe/H] < -4$ and hyper metal-poor (HMP) stars to $[Fe/H] < -5$. Some UMP stars are also carbon-enhanced metal-poor (CEMP) stars with $[C/Fe] > +1$.

4.2.1 ESO-LP and CEMP data

The ESO-LP contains 35 VMP stars, which includes 22 EMP stars. The star in their sample with the next to lowest iron abundance (CS 22949-037; $[Fe/H] = -3.97$) is a CEMP star. Note that CD-38°245 (Bessell & Norris 1984) has $[Fe/H]=-4.19$; unfortunately, Cayrel et al. (2004) and Bessell & Norris (1984) do not provide O abundances, and only an upper limit to the abundance of C. One result of this survey has been the reduction of the scatter in different element abundances as correlated against $[Fe/H]$ (e.g Mg, Ca, Cr and Ni). According to Beers & Christlieb (2005), this is contrary to the long-standing hypothesis that, at such low metallicity, one observes the nucleosynthetic products of only a few or even a single SN II (Shigeyama & Tsujimoto 1998; Tsujimoto et al. 2000). The lack of scatter in these abundances could be explained by a well-mixed ISM.

The CEMP stars references are retrieved from the SAGA tool² presented in Suda et al. (2008). Abundances derived from 1D and 3D model atmospheres and references are gathered in Table 1. At the lowest metallicity, HE 0107-5240 and HE 1327-2326 are both HMP and CEMP stars. The very specific chemical pattern of these stars is assumed to be related to the first stages of star formation. The UMP star HE 1300+0157 with $[Fe/H]=-3.88$ has an abundance pattern close to the single UMP star in the ESO-LP. For G77-61, the criterion of CEMP-no star is not strictly met (only an upper limit exists on $[Ba/Fe]$). Moreover, in contrast to the other stars considered, the abundances of G77-61 are based on medium resolution optical ($[Fe/H]$, $[C/Fe]$) and near-infrared ($[O/Fe]$) spectroscopy. This method can bring systematic uncertainties and possibly an over-estimate of C (Beers et al. 2007). Consequently, this star is

¹ For a given element X, the abundance relative to the solar value is defined by $[X/H] = \log_{10}(X/H) - \log_{10}(X/H)_{\odot}$.

² <http://saga.sci.hokudai.ac.jp/Retrieval/db.cgi>

Table 1. Abundances of CEMP stars

Name	[Fe/H] 1D/3D*	[C/H] 1D/3D	[O/H] 1D/3D
HE 1300+0157 ^a	-3.88 / -3.88	-2.50 / -3.10	-2.12 / -2.72
HE 1327-2326 ^b	-5.46 / -5.96	-1.55 / -2.18	-1.76 / -2.54
HE 0107-5240 ^c	-5.30 / -5.50	-1.30 / -2.30	-3.00 / -3.60
G-77-61 ^d	-4.00 / -4.20	-1.40 / -2.40	-2.20 / -2.80

Abundances derived from 1D and 3D model atmospheres * Abundances derived from 3D/NLTE model atmospheres are used for the main analysis (Section 5). Abundances derived from 1D model atmospheres are considered in Section 5.3.2.

^a assumed to be a subgiant as in Frebel et al. (2007).

^b Frebel et al. (2008).

^c Bessell et al. (2004); Christlieb et al. (2004); abundances derived from 3D model atmospheres are estimated from Collet et al. (2006).

^d Beers et al. (2007); Collet et al. (2006).

not used in the analysis, but is displayed in the figures for illustrative purposes. There is one additional star with $-5 < [\text{Fe}/\text{H}] < -4$, HE 0557-4840 (Norris et al. 2007). While it also has an enhanced C to Fe ratio, there is only an upper limit on [O/H] making it difficult to place this star directly into our analysis.

For our main analysis, abundances derived from 3D model atmospheres are considered first. We also discuss the impact of using 1D versus 3D model atmospheres in Section 5.3.2.

4.2.2 Transition discriminant

The transition from one star formation mode to another is often described in terms of a critical metallicity. For example, Bromm & Loeb (2003) have shown the importance of ionized carbon and neutral atomic oxygen in this transition and suggest that when sufficiently abundant, these elements act as a trigger to lower mass star formation. Frebel et al. (2007) defined the *transition discriminant*:

$$D_{\text{trans}} \equiv \log_{10}(10^{[\text{C}/\text{H}]} + 0.3 \times 10^{[\text{O}/\text{H}]}) . \quad (4)$$

It is argued that low-mass star formation requires $D_{\text{trans}} \gtrsim -3.5 \pm 0.2$ (Santoro & Shull 2006; Frebel et al. 2007). A scatter plot of D_{trans} as a function of [Fe/H] is shown in Fig. 4. All ESO-LP very metal-poor stars (circles) and CEMP stars meet the condition $D_{\text{trans}} \gtrsim -3.5$.

4.2.3 PopIII stars and the enrichment of CEMP stars

Our model follows C, O and Fe abundance evolution with z , and hence enables us to calculate D_{trans} and [Fe/H] at each redshift (see Section 2 for details and Daigne et al. 2006). In the D_{trans} versus [Fe/H] scatter plot of Fig. 4, the evolution from $z = 30$ to $z = 0$ corresponds to a continuous path starting at the lowest metallicity (left-hand side) and ending up at the highest metallicity (right-hand side).

A standard IMF used for the normal mode leads to the thick black-solid line. It reproduces well the ESO-LP observations, but it is clear that the CEMP stars abundances are not explained in this standard scenario. The evolution of D_{trans} in our best fit model (see next section) which includes a massive mode is shown as the red-dashed line. The SFR corresponding to this model is shown in Fig. 1 (red-dashed line) and corresponds to the parameters given above in Section 3.3.

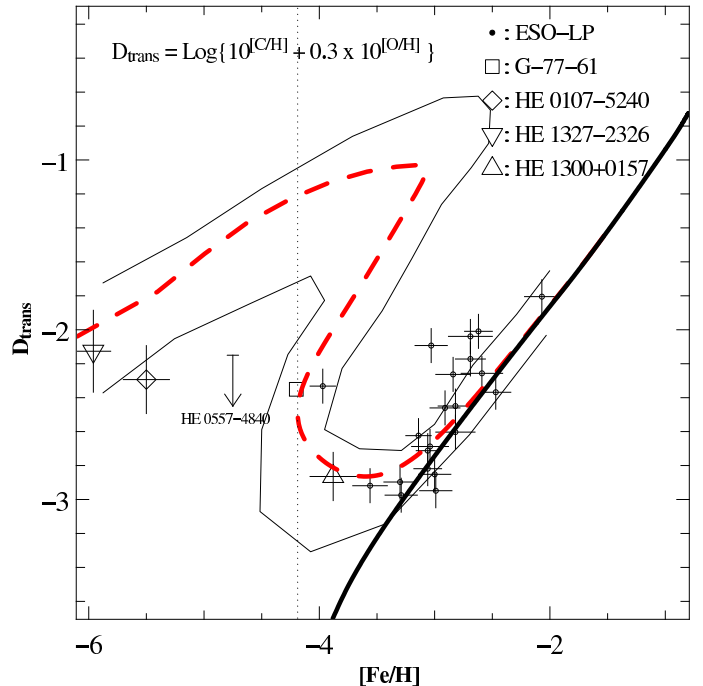


Figure 4. The transition discriminant, D_{trans} , for metal-poor stars as a function of [Fe/H]. The ESO-LP stellar data are shown as circles while peculiar CEMP stars are indicated with different symbols. The thick black solid line corresponds to a model with PopII/I stars alone. The addition of PopIII stars ($35\text{--}100 M_{\odot}$, our best model) leads to the red dashed line. The dotted vertical line indicates the prompt initial enrichment (PIE) produced by PopIII stars (see Fig. 3). The envelope (thin black curves) contains all evolution curves predicted by models, that match the abundance at a 95% CL, as determined by our χ^2 analysis (see Section 5). Only stars with error bars are included in this analysis.

PopIII SN eject more C and O than PopII/I yielding higher values of D_{trans} . This allows one to explain the abundances of the peculiar stars. As a result, these stars must be associated with star formation occurring within regions having a specific nucleosynthetic history at early times as suggested in Frebel (2008a). At intermediate redshift, we see a decrease of both D_{trans} and [Fe/H]. This corresponds to the epoch where the SFR is reduced (see Fig. 1). The accretion of pristine IGM material continues, leading to the dilution of ISM abundances. The abundance dilution allows one to reproduce simultaneously the observations of CEMP stars at high redshift and of ESO-LP stars at low redshift. As PopII/I stars turn on, we reconnect to the black solid line. Finally, the vertical dotted line indicates the PIE produced by PopIII stars as discussed already for the MDF drop in Section 4.1.

5 CONSTRAINTS ON POPIII STARS FROM LOCAL OBSERVATIONS

As shown above, PopII/I stars barely account for the reionization of the Universe. PopIII stars are not essential in this context, unless the SFR of PopII/I stars at $z > 7$ drops off faster than in our conservative choice (see Fig. 1), or the value of the escape fraction used in our study (20%) is overestimated. Conversely, if we turn to the local observations and interpret them in a cosmological context, PopIII stars are mandatory from chemical observations, especially based on the consideration of CEMP stars. Hence, if we consider that the abundances of CEMP stars are representative of the nucle-

osynthesis of the first stars, we can perform a statistical analysis to constrain the PopIII parameters. We have shown above that the few stars observed at very low metallicities are not sufficient to use the MDF as a constraint on PopIII models. To reproduce the slope of the MDF at $[\text{Fe}/\text{H}] > -3.5$, we consider only minimal masses of 30-40 M_{\odot} for PopIII stars.

We first describe the method to evaluate the quality of the model. In this process, a redshift of formation can be set to each observed star. We then discuss the constraints set by abundances derived from 3D model atmospheres and the uncertainties related to 1D or 3D model atmospheres.

5.1 Methodology

The analysis is done in the $D_{\text{trans}}-[\text{Fe}/\text{H}]$ plane, using a grid approach to cover the parameter space of the model. The parameters that we vary are ν_{III} (from 2×10^{-5} to $2 \times 10^{-2} M_{\odot} \text{ yr}^{-1} \text{ Mpc}^{-3}$), $z_{m\text{III}}$ (from 10 to 26), a_{III} (from 0.5 to 5), b_{III} (from 0.03 to 4.9) and the minimum mass of the massive mode, M_{III} (from 30 to 39 M_{\odot}).

5.1.1 Minimization procedure

For each model, we calculate the $D_{\text{trans}}-[\text{Fe}/\text{H}]$ curve, which is multi-valued for models including PopIII stars. The best fit model corresponds to the set of parameters that minimizes a χ^2 on the predicted and observed stellar iron abundance and transition discriminant D_{trans} (via stellar carbon and oxygen abundances) of a sample of 21 ESO-LP and 3 peculiar stars. We consider all parameters within a 95% confidence level (CL) based on this χ^2 to be acceptable. Therefore, in all figures, we have displayed 95% CL envelopes that contain the predicted curves of all those acceptable models.

5.1.2 Transforming stellar abundances to redshift

In many models, the iron abundance is monotonically increasing with time, giving a unique correspondance between $[\text{Fe}/\text{H}]$ and redshift. This is the classical view of cosmological chemical evolution, where the oldest stars are the most metal-poor. However, in the first metal-free structures, the nucleosynthesis of PopIII stars provide features in the evolution of $[\text{Fe}/\text{H}]$, so that the previous picture does not necessarily hold. In that case, not only the abundances of Fe, but also of elements such as C and O are required in order to be able to assign the VMP stars to a particular redshift.

Each position along the predicted curve $D_{\text{trans}}/[\text{Fe}/\text{H}]$ is associated with a redshift. Following the procedure described above, we search for the position along this curve that minimizes the distance to the observed values for a given star. This position gives the redshift of formation of this star. The predicted curve depends on the model considered, and therefore different models will associate different redshifts of formation with the same star. As we repeat this procedure for models that satisfy the 95% CL on the whole sample, we can infer the allowed range of redshift (from the minimum to the maximum redshift) for one specific star.

5.2 abundances derived from 3D model atmospheres

Models that satisfy a 95% CL limit are included within the envelope shown in Fig. 4 (thin black lines). All stars included in our

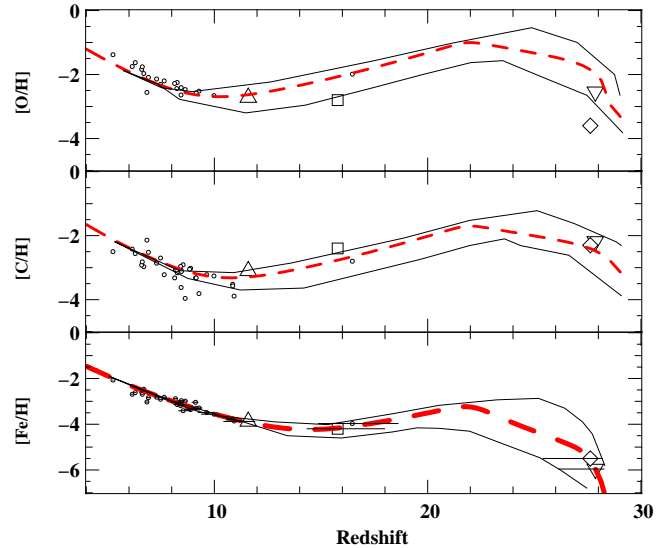


Figure 5. Evolution of the $[\text{Fe}/\text{H}]$, $[\text{C}/\text{H}]$ and $[\text{O}/\text{H}]$ abundances with redshift. Dashed red curves and black solid lines correspond to the prediction from the best model and to the 95% CL envelopes (Section 5). The SFR of the best model is shown in Fig. 1. Symbols used for the stars are the same as in Fig. 4. Horizontal lines in the bottom panel give the estimated errors on redshift for CEMP stars (Table 2).

analysis are located along the path defined by the best fit. As explained in Section 4.2, G77-61 displays larger errors on its abundance determination. Yet, it is also located within the envelope (square in Fig. 4). HE 0557-4840 is located at a somehow low value for $[\text{Fe}/\text{H}]$. According to the exact value for D_{trans} , it could either seat outside the envelope ($D_{\text{trans}} \simeq -2.2$) or be very close to the edge ($D_{\text{trans}} \simeq -3$).

5.2.1 Consequence for SFR and optical depth

The envelope of the PopIII SFR for all allowed models is shown in Fig. 1 (shaded area). Some common features can be noted: the massive mode becomes sub-dominant for redshift lower than about 15; on the contrary, it is required at a level of $2 \times 10^{-4} - 3 \times 10^{-3} M_{\odot} \text{ yr}^{-1} \text{ Mpc}^{-3}$ around $z \sim 24 - 28$. The PopIII SFR cannot be larger than $3 \times 10^{-3} M_{\odot} \text{ yr}^{-1} \text{ Mpc}^{-3}$ independently of the redshift.

The envelope of the optical depth history among all models is shown in Fig. 2 (light shaded area). We verify that all models are compatible with the 1σ limit of WMAP5.

5.2.2 Redshift of formation

As explained in Section 5.1.2, for a given model, we have assigned a typical redshift, z_* , of formation to each individual star. Thus, we can locate each star on a plot of abundances versus redshift, and compare them directly to the predicted evolution. This is done in Fig. 5 using the best fit model (dashed red line). We also show the corresponding 95% CL envelopes for the evolution of the abundances (thin black lines). Those envelopes also bracket the errors on the redshift of formation (see $[\text{Fe}/\text{H}]$ plot in Fig. 5). The redshift ranges are given in Table 2.

We see that CEMP stars are likely to form at high redshift. For example, the star HE 1300+0157 (upper triangle in Fig. 4) is found to be formed at $z_* \sim 11$ (for the best fit model). HE 1300+0157

is located along a branch of the evolution where the dilution by IGM accretion is the only important process. Then, abundances decrease very slowly and uncertainties on the redshift are of the order of 100 Myr ($15 < z < 20$). It is interesting to note that the predicted abundances also reproduce the Fe, C and O abundances at this specific redshift. The star G 77-61 (square), that has a similar iron abundance but a higher carbon abundance, is born earlier (it is located on a different place along the curve $D_{\text{trans}}\text{-}[\text{Fe}/\text{H}]$; Fig. 4) at $z \sim 16$. The exact redshift for HE 1327-2326 and HE 0107-5240 (lower triangle and diamond) depends on the exact time of formation of the first structure, which is largely unknown. The duration of this episode is only a few tens of Myr, which also corresponds to the uncertainty on the redshift of formation of those stars. Finally, all stars observed in the ESO-LP are found to form at redshift below 10, except CS 22949-037 whose abundances are very similar to HE 1300+0157 (Section 4.2).

5.3 Uncertainties

5.3.1 Peculiar stars

The observed oxygen abundance in the UMP star HE 0107-5240 (diamond in upper panel of Fig. 5) seems to be lower than the predicted abundances. This discrepancy points to the very special stars where C, O abundances are not explained by standard predictions (Nomoto et al. 2006; Tominaga et al. 2007). It is clear that the yields of the massive stars at zero metallicity are poorly known. For example, new calculations concerning the effect of rotation on the evolution of primordial stars can modify considerably the abundance of C and O, and their corresponding ratio (Ekström et al. 2008). They would then allow for a decrease of about 1 dex required for the oxygen abundance of HE 0107-5240 to be reproduced.

5.3.2 1D vs 3D model atmospheres

We now study the influence of uncertainties on stellar abundances on the overall results. We have performed the same full analysis using the abundances derived from 1D model atmospheres (given in Table 1), yielding new envelopes for the $D_{\text{trans}}\text{-}[\text{Fe}/\text{H}]$ plane, abundance evolution, optical depth evolution and SFR of PopIII stars. In the following figures, the same symbols as above are used for each CEMP star. We do not show ESO-LP stars in the figures, as their positions are unchanged.

The main effect of the correction applied to abundances derived from 1D model atmospheres is to lower all abundances by about 0.1 dex for $[\text{Fe}/\text{H}]$, and up to 1 dex for C and O abundances. This can be seen in Fig. 6 by comparing filled and open symbols (abundances derived from 3D and 1D model atmospheres respectively). Given the predicted path of $D_{\text{trans}}\text{-}[\text{Fe}/\text{H}]$, this does not modify much the envelope in the intermediate redshift range. At high redshift, the effect is strong and displaces the envelope towards lower values of D_{trans} . In both cases, PopIII stars are required and a very similar pattern is displayed.

As for the SFR, the best fit model assuming abundances derived from 1D model atmosphere extends slowly down to about $10^{-7} M_{\odot} \text{ yr}^{-1} \text{ Mpc}^{-3}$ at $z \sim 4$. However, the global envelope (including all possible shapes) is almost identical in both cases, although a bit more extended assuming 1D model atmospheres. The evolution of optical depth is also not modified in a significant way, since the contribution of PopIII stars to reionization is marginal.

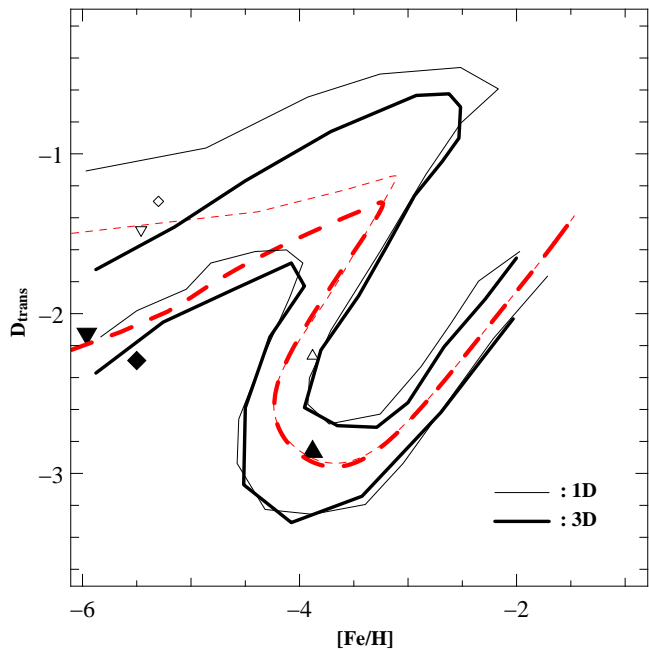


Figure 6. The transition discriminant, D_{trans} , as a function of $[\text{Fe}/\text{H}]$ (same as Fig. 4). The abundances of CEMP stars derived from 1D and 3D model atmospheres (Table 1) are marked with filled and open symbols respectively. The 95% CL envelopes of predicted evolution assuming 3D and 1D model atmospheres are displayed with thick and thin solid lines respectively, while best models are shown with thick and thin dashed lines.

Table 2. Estimation of the redshift of formation of CEMP stars

Name	3D model ^b			1D model ^b		
	z_{min}^a	z_{best}	z_{max}^a	z_{min}^a	z_{best}	z_{max}^a
HE 1300+0157	10.4	11.6	11.9	9.7	11.5	12.0
HE 1327-2326	26.1	27.9	28.3	24.9	28.3	28.4
HE 0107-5240	25.4	27.6	28.2	24.7	28.3	28.3
G-77-61	14.3	15.8	18.0	14.3	15.9	19.5

^a Minimum and maximum redshift predicted by models that match abundances of all stars at a 95% CL (Section 5). ^b Abundances are derived from 3D model atmospheres (second to fourth columns) or from 1D model atmospheres (fifth to last columns).

Finally, we consider how our estimates for the redshift of formation of CEMP stars are affected. Fig. 7 displays the envelope for the evolution of abundances with redshift allowed in the two cases. It appears even more clearly that the discrepancy occurs only at high redshift, while the transition from CEMP to standard metal-poor stars is required in both cases. The stars are not located in this figure for clarity. The different ranges of estimates for their redshift of formation are summarised in Table 2. Again, only the two stars at the highest redshift are affected by this uncertainty; while the range of allowed redshift is larger in the case of abundances derived from 1D model atmospheres (this is not visible in Fig. 7).

6 DISCUSSION AND CONCLUSIONS

Following the approach developed in Daigne et al. (2004), we have modeled the evolution of individual element abundances in the ISM assuming homogeneous star formation and stellar yields. Recent observations at $z \sim 7-8$ (Bouwens et al. 2007) were used to better

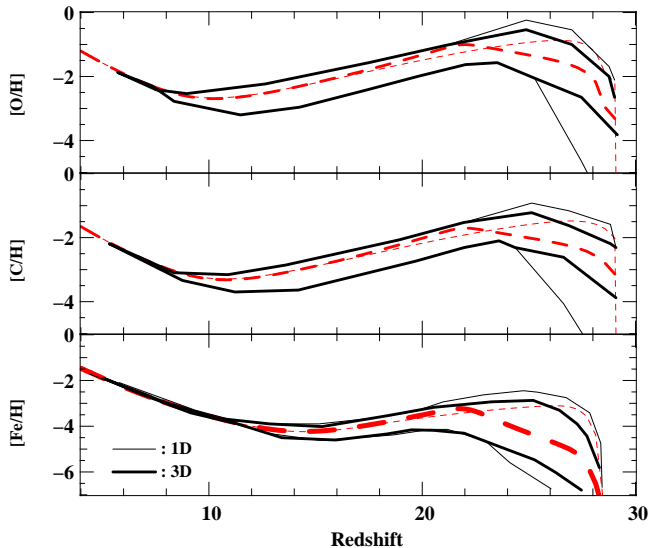


Figure 7. Evolution of the $[\text{Fe}/\text{H}]$, $[\text{C}/\text{H}]$ and $[\text{O}/\text{H}]$ abundances with redshift (same as in Fig. 5). The 95% CL envelopes of allowed evolutions assuming abundances derived from 3D and 1D model atmospheres for CEMP stars are displayed with thick and thin lines respectively. The envelope as well as the evolution for the best models (thick and thin dashed red lines) are quite different at high redshift only.

constrain one ingredient of the model, namely the SFR for PopII/I at high redshift. We have shown that a homogeneous scenario of hierarchical structure formation reproduces many different observations, from reionisation and first star abundances to local abundance observations. We found that using the most recent results on the optical depth from WMAP, a massive mode is not absolutely required. Nevertheless, the data can accommodate a PopIII contribution, responsible for the gradual reionization starting from $z \simeq 20$. Although the cosmological importance of PopIII stars cannot be fully constrained by the integrated Thomson optical depth, this question may be better tackled in the future with the help of accurate measurements of the CMB polarization data (Dunkley et al. 2009).

We have also considered stellar constraints, in particular the MDF and the evolution of D_{trans} with $[\text{Fe}/\text{H}]$. In the literature, the slope of the MDF can be reproduced by different models of chemical enrichment, from galactic models to hierarchical analytic models including merger trees, as shown in Fig. 12 of Schoerck et al. (2008) (see also Tumlinson 2006). This indicates that the slope of the MDF does not discriminate between the methods used and the associated level of heterogeneity. In contrast, the pattern at $[\text{Fe}/\text{H}] < -3.5$ is more difficult to reproduce. Schoerck et al. (2008) claim that no model considered in their paper can reproduce the MDF at very low iron abundances. We find that the modification of the tail at low values of $[\text{Fe}/\text{H}]$ may be related to the presence of PopIII stars. In our study, we have tested the impact of the massive mode by varying the typical PopIII minimal mass from 8 to $40 M_{\odot}$. This appears to be an important parameter as found in the study of Salvadori et al. (2007). They used a mass range from 140 to $200 M_{\odot}$ which we consider disfavoured by the very specific yields of the stars within this mass range (Daigne et al. 2006). In this paper, we demonstrate that the minimum mass must be larger than about $30 M_{\odot}$ in order to reproduce the observed part of the MDF.

We have shown that the existence of PopIII stars at high red-

shift is required to explain the abundance pattern observed in the CEMP stars. In addition, we have shown that a massive mode with a typical mass of $40 M_{\odot}$ reproduces the evolution of observed D_{trans} . In contrast, it is known that PISN with masses $140\text{--}200 M_{\odot}$ do not provide the correct chemical pattern and cannot reach high values of D_{trans} for low values of $[\text{Fe}/\text{H}]$ (the ratio C/Fe in their yields, Heger et al. 2003, is not high enough). However, if it could be established that the CEMP stars were particular cases, such as belonging to binaries (Ryan et al. 2005; Tumlinson 2007) or due to the preferential depletion of iron in grains (Venn & Lambert 2008), the SFR related to PopIII stars would be diminished, at least as far as chemical evolution is concerned.

In conclusion, our analysis hints at a massive mode at $z \simeq 20 - 30$, which becomes sub-dominant at lower z ($z \sim 15$).

Going further requires improvements from the observational and theoretical point of view. On the theoretical part, the existence of PopIII stars with masses of a few tens of solar masses is also suggested by recent hydrodynamical simulations (Bromm & Loeb 2003; Greif & Bromm 2006; Johnson & Bromm 2006, 2007; Johnson et al. 2007; Yoshida et al. 2007; Greif et al. 2008; Smith et al. 2009). The explosion of these high mass stars disrupts the surrounding environment and delays the formation of lower mass stars *within the same structure*. Merger trees (Salvadori et al. 2007) account for such a mechanical feedback which delays PopII/I star formation along a single branch. In a homogeneous picture, this delay translates into a reduction of the SFR between the two modes. We note that this epoch is very short in our model (100–200 Myr). However, the exact evolution of the structures are still uncertain. One also needs improved yields provided by stellar evolution models at all metallicities and, more specifically, SN calculations that are even more uncertain. Note however that uncertainties related to the determination of abundances (derived from 1D or 3D model atmospheres) do not change our conclusion on the cosmological importance of PopIII stars.

Many improvements are possible in the future with regard to observations. (i) Additional stellar constraints and abundance measurements. Better statistics are necessary to construct the MDF at very low metallicity, with next generation optical telescopes such as GMT. It will then be possible to constrain in a better way the epoch of the massive population (whose duration is related to the critical metallicity as used in merger trees; Salvadori et al. 2007; Tumlinson 2006) and the typical mass range of PopIII stars. (ii) More complete spectroscopic observations in very metal-poor stars are needed in order to obtain a complete set of observations in the D_{trans} diagram. Of particular importance is the continued search for HMP stars and UMP stars to test their statistical significance relative to the bulk of the VMP/EMP stars. (iii) In future studies, one could attempt to better constrain the model using other chemical elements, in particular r and s-process elements which can bring new constraints on the mass range of massive stars, PopIII (e.g. Frebel 2008b). (iv) Additional cosmological constraints at high redshift. Massive objects may be directly observable, as more and more quasars and galaxies are detected at high redshift (Fan et al. 2003; Kneib et al. 2004; Iye et al. 2006) and with JWST in the future (e.g. Stiavelli & Trenti 2009). However, the extreme brevity of the PopIII epoch makes the connection unclear (Alvarez et al. 2007). A more promising probe would be the observations of high redshift gamma-ray bursts, that correspond, for the longer bursts, to the deaths of massive single stars (Heger et al. 2003; Barton et al. 2004; Bromm & Loeb 2006; Daigne et al. 2006). Recent observations of GRBs at $z > 6$ (GRB 050904 at $z = 6.3$, Kawai et al.

2006; GRB 080913 at $z = 6.7$, Greiner et al. 2009) and even $z > 8$ (GRB 090423 at $z \sim 8.2$, Tanvir et al. 2009) are extremely encouraging. (*v*) In addition, massive stars would have polluted their environment with an initial enrichment of heavy elements which could be compared to the one observed in the Ly α forest along quasar absorption spectra at $z \lesssim 6$ (Songaila 2001; Aguirre et al. 2002; Aracil et al. 2004) or in the Damped Lyman α systems (Ledoux et al. 2003; Prochaska et al. 2003). This requires a better understanding of the outflows of metals into the IGM which is beyond the scope of this work. In addition, it will be important to better understand the role of inhomogeneities on the different populations of the first stars. The uniformity and extent of the metal pollution is also under debate, and could in the future be used to distinguish between local and recent pollution and global pollution by an earlier population of stars (Madau et al. 2001; Mori et al. 2002; Wada & Venkatesan 2003).

ACKNOWLEDGMENTS

We are very grateful to Roger Cayrel and Patrick Petitjean for their always pertinent and fruitful comments. We also thank Sylvia Ekström for useful discussions on the yields of PopIII stars. We thank the referee very much for a very careful reading and advice specifically regarding observational aspects. We thank E. Thiébaud, and D. Munro for freely distributing his Yorick programming language (<http://yorick.sourceforge.net/>), which we used to implement our analysis. The work of E.V. and K.A.O. has been supported by the collaboration INSU-CNRS France/US. The work of K.A.O. was partially supported by DOE grant DE-FG02-94ER-40823.

REFERENCES

- Aguirre A., Schaye J., Theuns T., 2002, ApJ, 576, 1
 Alvarez M. A., Wise J., Abel T., 2007, Bulletin of the American Astronomical Society, 38, 885
 Aracil B., Petitjean P., Pichon C., Bergeron J., 2004, A&A, 419, 811
 Bagla J. S., Kulkarni G., Padmanabhan T., 2009, MNRAS, 397, 971
 Barton E. J., Davé R., Smith J.-D. T., Papovich C., Hernquist L., Springel V., 2004, ApJ, 604, L1
 Beers T. C., Christlieb N., 2005, ARA&A, 43, 531
 Beers T. C., Sivarani T., Marsteller B., Lee Y., Rossi S., Plez B., 2007, AJ, 133, 1193
 Bessell M. S., Christlieb N., Gustafsson B., 2004, ApJ, 612, L61
 Bessell M. S., Norris J., 1984, ApJ, 285, 622
 Bouwens R. J., Illingworth G. D., Franx M., Ford H., 2007, ApJ, 670, 928
 Bromm V., Larson R. B., 2004, ARA&A, 42, 79
 Bromm V., Loeb A., 2003, Nature, 425, 812
 Bromm V., Loeb A., 2006, ApJ, 642, 382
 Cayrel R., Depagne E., Spite M., et al., 2004, A&A, 416, 1117
 Christlieb N., Gustafsson B., Korn A. J., et al., 2004, ApJ, 603, 708
 Christlieb N., Schörck T., Frebel A., Beers T. C., Wisotzki L., Reimers D., 2008, A&A, 484, 721
 Collet R., Asplund M., Trampedach R., 2006, ApJ, 644, L121
 Daigne F., Olive K. A., Silk J., Stoehr F., Vangioni E., 2006, ApJ, 647, 773
 Daigne F., Olive K. A., Vangioni-Flam E., Silk J., Audouze J., 2004, ApJ, 617, 693
 Daigne F., Rossi E. M., Mochkovitch R., 2006, MNRAS, 372, 1034
 Dunkley J., Komatsu E., Nolta M. R., et al., 2009, ApJS, 180, 306
 Ekström S., Meynet G., Chiappini C., Hirschi R., Maeder A., 2008, A&A, 489, 685
 Fan X., Strauss M. A., Schneider D. P., et al., 2003, AJ, 125, 1649
 Faucher-Giguère C.-A., Lidz A., Hernquist L., Zaldarriaga M., 2008, ApJ, 682, L9
 Frebel A., 2008a, New Horizons in Astronomy: ASP Conference Series, Edited by Anna Frebel, Justyn R. Maund, Juntai Shen, and Michael H. Siegel. San Francisco: Astronomical Society of the Pacific, 393, 63
 Frebel A., 2008b, ArXiv e-prints 0812.1227
 Frebel A., Collet R., Eriksson K., Christlieb N., Aoki W., 2008, ApJ, 684, 588
 Frebel A., Johnson J. L., Bromm V., 2007, MNRAS, 380, L40
 Frebel A., Norris J. E., Aoki W., Honda S., Bessell M. S., Takada-Hidai M., Beers T. C., Christlieb N., 2007, ApJ, 658, 534
 Frebel A., Simon J. D., Geha M., Willman B., 2009, ArXiv e-prints 0902.2395
 Greif T. H., Bromm V., 2006, MNRAS, 373, 128
 Greif T. H., Johnson J. L., Bromm V., 2008, First Stars III: AIP Conference Series, 990, 405
 Greif T. H., Johnson J. L., Klessen R. S., Bromm V., 2008, MNRAS, 387, 1021
 Greiner J., et al., 2009, ApJ, 693, 1610
 Heger A., Fryer C. L., Woosley S. E., Langer N., Hartmann D. H., 2003, ApJ, 591, 288
 Heger A., Woosley S. E., 2008, ArXiv e-prints 0803.3161
 Henriques B. M. B., Thomas P. A., Oliver S., Roseboom I., 2009, MNRAS, 396, 535
 Hopkins A. M., Beacom J. F., 2006, ApJ, 651, 142
 Iye M., Ota K., Kashikawa N., et al., 2006, Nature, 443, 186
 Jenkins A., Frenk C. S., White S. D. M., et al., 2001, MNRAS, 321, 372
 Johnson J. L., Bromm V., 2006, MNRAS, 366, 247
 Johnson J. L., Bromm V., 2007, MNRAS, 374, 1557
 Johnson J. L., Greif T. H., Bromm V., 2007, ApJ, 665, 85
 Johnson J. L., Greif T. H., Bromm V., Klessen R. S., Ippolito J., 2009, ArXiv e-prints 0902.3263
 Kampakoglou M., Trotta R., Silk J., 2008, MNRAS, 384, 1414
 Karlsson T., 2006, ApJ, 641, L41
 Kawai N., et al., 2006, Nature, 440, 184
 Kirby E. N., Simon J. D., Geha M., Guhathakurta P., Frebel A., 2008, ApJ, 685, L43
 Kneib J.-P., Ellis R. S., Santos M. R., Richard J., 2004, ApJ, 607, 697
 Komiya Y., Suda T., Fujimoto M. Y., 2009, ApJ, 694, 1577
 Ledoux C., Petitjean P., Srianand R., 2003, MNRAS, 346, 209
 Madau P., Ferrara A., Rees M. J., 2001, ApJ, 555, 92
 Maeder A., Meynet G., 1989, A&A, 210, 155
 Mori M., Ferrara A., Madau P., 2002, ApJ, 571, 40
 Nagao T., Sasaki S. S., Maiolino R., et al., 2008, ApJ, 680, 100
 Nomoto K., Tominaga N., Umeda H., Kobayashi C., Maeda K., 2006, Nuclear Physics A, 777, 424
 Norris J. E., Christlieb N., Korn A. J., et al., 2007, ApJ, 670, 774
 Oesch P. A., Carollo C. M., Stiavelli M., et al., 2009, ApJ, 690, 1350
 Press W. H., Schechter P., 1974, ApJ, 187, 425

- Prochaska J. X., Gawiser E., Wolfe A. M., Castro S., Djorgovski S. G., 2003, *ApJ*, 595, L9
- Ryan S. G., Aoki W., Norris J. E., Beers T. C., 2005, *ApJ*, 635, 349
- Salvadori S., Schneider R., Ferrara A., 2007, *MNRAS*, 381, 647
- Santoro F., Shull J. M., 2006, *ApJ*, 643, 26
- Schaerer D., 2002, *A&A*, 382, 28
- Schoerck T., Christlieb N., Cohen J. G., et al., 2008, *ArXiv e-prints* 0809.1172
- Sheth R. K., Tormen G., 1999, *MNRAS*, 308, 119
- Shigeyama T., Tsujimoto T., 1998, *ApJ*, 507, L135
- Smith B. D., Turk M. J., Sigurdsson S., O'Shea B. W., Norman M. L., 2009, *ApJ*, 691, 441
- Songaila A., 2001, *ApJ*, 561, L153
- Spiegel D. N., Bean R., Doré O., et al., 2007, *ApJS*, 170, 377
- Springel V., Hernquist L., 2003, *MNRAS*, 339, 312
- Stiavelli M., Trenti M., 2009, in *Bulletin of the American Astronomical Society Vol. 41 of Bulletin of the American Astronomical Society, Observing First Light With JWST: An Update.* pp 255–+
- Suda T., Katsuta Y., Yamada S., Suwa T., Ishizuka C., Komiya Y., Sorai K., Aikawa M., Fujimoto M. Y., 2008, *PASJ*, 60, 1159
- Tanvir N. R., Fox D. B., Levan et al., 2009, *ArXiv e-prints* 0906.1577
- Tominaga N., Umeda H., Nomoto K., 2007, *ApJ*, 660, 516
- Trenti M., Stiavelli M., 2009, *ApJ*, 694, 879
- Tsujimoto T., Shigeyama T., Yoshii Y., 2000, *ApJ*, 531, L33
- Tumlinson J., 2006, *ApJ*, 641, 1
- Tumlinson J., 2007, *ApJ*, 665, 1361
- van den Hoek L. B., Groenewegen M. A. T., 1997, *A&AS*, 123, 305
- Venn K. A., Lambert D. L., 2008, *ApJ*, 677, 572
- Wada K., Venkatesan A., 2003, *ApJ*, 591, 38
- Woosley S. E., Weaver T. A., 1995, *ApJS*, 101, 181
- Yoshida N., Oh S. P., Kitayama T., Hernquist L., 2007, *ApJ*, 663, 687